ARTICLES
PUBLISHED ONLINE: 7 JULY 2013 | DOI: 10.1038/NMAT3700
nature materials

Enhanced catalytic activity in strained chemically exfoliated WS_2 nanosheets for hydrogen evolution

Damien Voiry[1], Hisato Yamaguchi[1], Junwen Li[2], Rafael Silva[3], Diego C. B. Alves[1], Takeshi Fujita[4], Mingwei Chen[4], Tewodros Asefa[3,5], Vivek B. Shenoy[2], Goki Eda[6,7] and Manish Chhowalla[1]*

Efficient evolution of hydrogen through electrocatalysis at low overpotentials holds tremendous promise for clean energy. Hydrogen evolution can be easily achieved by electrolysis at large potentials that can be lowered with expensive platinum-based catalysts. Replacement of Pt with inexpensive, earth-abundant electrocatalysts would be significantly beneficial for clean and efficient hydrogen evolution. To this end, promising results have been reported using 2H (trigonal prismatic) XS_2 (where X = Mo or W) nanoparticles with a high concentration of metallic edges. The key challenges for XS_2 are increasing the number and catalytic activity of active sites. Here we report monolayered nanosheets of chemically exfoliated WS_2 as efficient catalysts for hydrogen evolution with very low overpotentials. Analyses indicate that the enhanced electrocatalytic activity of WS_2 is associated with the high concentration of the strained metallic 1T (octahedral) phase in the as-exfoliated nanosheets. Our results suggest that chemically exfoliated WS_2 nanosheets are interesting catalysts for hydrogen evolution.

Realization of the hydrogen economy will require efficient and sustainable production of hydrogen. The scientific community has been actively searching for new electrocatalysts that decrease the overpotential of the hydrogen evolution reaction[1–10] (HER, $2H^+ + 2e^- \rightarrow H_2$) as well as being earth abundant and inexpensive[1,7,11–16]. Platinum is the most electroactive and electrochemically stable catalyst, making it challenging to find a suitable replacement. The identification of XS_2 compounds as potential efficient catalysts for HER has opened up an exciting new path for the field[3–6,16,17]. Much of the experimental work has stemmed from theory that suggested that metallic edges[11] of 2H XS_2 crystals are electrocatalytically active[3]. This has led to investigations of XS_2 nanoparticles or complexes with a high concentration of exposed edges as electrocatalysts for hydrogen evolution[5,15–19]. Further improvements in the HER kinetics by placing XS_2 nanoparticles on a variety of substrates including reduced graphene oxide have also been observed[20]. XS_2 compounds belong to the layered transition-metal dichalcogenides (LTMDs) family of compounds that have a lamellar structure comparable to graphite in which the individual S-metal-S layers weakly interact with each other. Similar to graphite, LTMDs can be exfoliated into their individual atomically thin sheets by mechanical, chemical or electrochemical means[21–24]. Liquid-based exfoliation of layered compounds has been known and studied over several decades but recently received renewed interest with the work of ref. 24. In addition to chemical exfoliation, chemical vapour deposition of ultrathin XS_2 layers has also been achieved[25–27]. Recently, layers deposited on nickel foams by this method have been investigated for hydrogen evolution[28]. The ease of fabrication along with high carrier mobility[29] and interesting optical properties[23,30,31] makes single layered LTMDs attractive for a wide variety of opto-electronic applications but their catalytic properties remain largely unexplored.

We have recently used a well-established lithium intercalation chemical method[21] to efficiently exfoliate MoS_2 into monolayered nanosheets[32] and deposit uniform thin films from them. The as-exfoliated nanosheets predominantly consist of 1T structure that is metallic[33], in contrast to the semiconducting 2H phase (Supplementary Information). The 1T phase is metastable so that annealing of as-exfoliated sheets results in restoration of the 2H phase, which is accompanied by a metallic to semiconducting electronic transition[34]. The bandgap of the annealed 2H phase is ~2.0 eV, ideal for photocatalysis[35]. In this study, we have explored the electrocatalytic properties for HER of atomically thin WS_2 nanosheets.

To prepare the nanosheets, commercially available WS_2 powder was lithium intercalated to form Li_xWS_2, which can be readily exfoliated through forced hydration to form a stable suspension[36] (Methods). The electrodes for HER were prepared by drop-casting a fixed volume and concentration of WS_2 sheets from an aqueous suspension onto glassy carbon. We have verified using Rutherford backscattering spectroscopy that the exfoliated samples are chemically pure and do not contain measurable lithium impurities (Supplementary Fig. S11). A typical atomic force microscopy (AFM) image of exfoliated XS_2 nanosheets deposited by drop-casting is shown in Fig. 1a. Analyses of AFM images revealed that most flakes have lateral dimensions in the 100–800 nm range and a thickness of ~1 nm.

The structure of chemically as-exfoliated XS_2 has been studied in detail and it is agreed that it departs from an ideal 1T structure of TiS_2 (ref. 34). Through a series of careful and detailed studies, it has been concluded that the structure can be described as a

[1]Rutgers University, Materials Science and Engineering, 607 Taylor Road, Piscataway, New Jersey 08854, USA, [2]University of Pennsylvania, Materials Science and Engineering, 3231 Walnut Street, Philadelphia, Pennsylvania 19104, USA, [3]Rutgers University, Department of Chemistry and Chemical Biology, 610 Taylor Road, Piscataway, New Jersey 08854, USA, [4]WPI Advanced Institute for Materials Research, Tohoku University, Sendai 980-8577, Japan, [5]Rutgers University, Department of Chemical and Biochemical Engineering, 98 Brett Road, Piscataway, New Jersey 08854, USA, [6]National University of Singapore, Physics Department and Graphene Research Centre, 2 Science Drive 3, Singapore 117542, Singapore, [7]National University of Singapore, Chemistry Department, 3 Science Drive 3, Singapore 117543, Singapore. *e-mail: manish1@rci.rutgers.edu

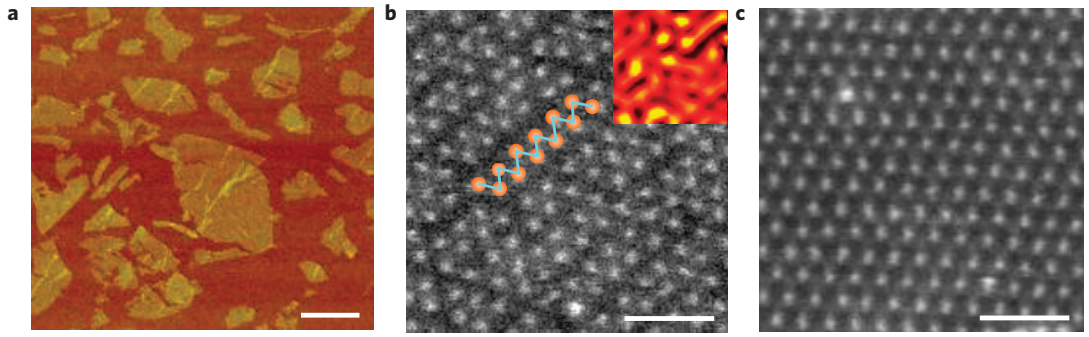

Figure 1 | Structure of chemically exfoliated WS_2. a, Typical AFM image of individual exfoliated nanosheets of XS_2 (where X = Mo or W). Scale bar, 500 nm. **b**,**c**, High-resolution STEM images of an as-exfoliated WS_2 monolayer showing regions exhibiting the 1T superlattice (**b**) and 2H structures (**c**). The inset in **b** shows the strain tensor map generated from the STEM-HAADF image using peak pair analysis. Light (yellow) and dark (black) colours correspond to regions where the strain is in tension and compression, respectively. Scale bars, 1 nm.

highly distorted 1T structure with a $2a_0 \times a_0$ superlattice[34,37]. We have used high-angle annular dark field (HAADF) imaging in an aberration-corrected scanning transmission electron microscope (STEM) to demonstrate that the structure of as-exfoliated WS_2 consists primarily of disordered superlattice regions (Fig. 1b). On annealing, the 1T phase relaxes to the stable 2H structure as shown in Fig. 1c. The superlattice structure is the distorted and strained 1T phase that is well known to develop during Li intercalation[34]. The corresponding schematics of the distorted 1T and 2H phases are shown in Supplementary Fig. S1 to help visualize the atomic structure. The STEM-HAADF image in Fig. 1b is the first direct observation of the zigzag pattern that was previously inferred through spectroscopic and diffraction techniques for chemically exfoliated MoS_2 and WS_2 (ref. 37). For the zigzag chain superlattice regions, we observe two distinct W–W distances, 2.7 Å and 3.3 Å, that are substantially different from 3.15 Å for pristine 2H WS_2.

The presence of the zigzag structure in Fig. 1b indicates a large concentration of locally strained bonds. We analysed the images using peak pair analysis[38] to obtain a strain tensor map of the 1T structure (Methods). The inset in Fig. 1b shows the corresponding strain tensor map of mean dilatation $[\Delta_{ij} = 1/2(\partial u_i/\partial x_i + \partial u_j/\partial x_j)]$. A complete stress tensor map is provided in Supplementary Fig. S2. It can be seen that frequent occurrence of kinks in the zigzag chains leads to strong deformation and regions of high local strain, which gives rise to an overall isotropic strain. The net change in the lattice parameter has been suggested to be ~3% by X-ray diffraction analysis[39], which is comparable to what we have observed by STEM-HAADF. We have also correlated the STEM-HAADF observations with Raman and X-ray photoelectron spectroscopic (XPS) analyses, revealing the presence of the metallic 1T phase in the as-exfoliated nanosheets (Supplementary Fig. S3).

The HER with a monolayer of WS_2 nanosheet thin film as the catalyst on glassy carbon was measured using the standard three-electrode electrochemical configuration in 0.5 M H_2SO_4 electrolyte de-aerated with Ar, as described in the Methods. The electrodes were prepared by depositing 0.1–0.2 μg cm^{-2} or approximately one continuous layer of WS_2 nanosheets over the electrode surface area (Methods). The polarization curves (not *iR* corrected) showing the normalized current density versus voltage (j versus V) for the 1T and 2H films along with Pt and bulk WS_2 powder samples, for comparison, are shown in Fig. 2a. In addition, a sub-monolayered film of as-exfoliated WS_2 nanosheets is also shown in Fig. 2a. It can be seen from the inset in Fig. 2a that for the as-exfoliated WS_2 thin-film electrodes the reaction begins at exceptionally low cathodic voltages ranging from 30 to 60 mV (which gives overpotential values of 80–100 mV), above which the current increases rapidly. The overpotential and the Tafel slopes are slightly higher in the case of sub-monolayered WS_2 thin films, which is attributed to poor charge transfer from the film to the electrode[20]. That is, below the percolation threshold, transport through the sheets is poor and thus the overall conductance is low, which limits charge transfer and the catalytic activity. The 2H WS_2 electrodes show HER characteristics that are consistent with MoS_2 edges[4,6,18,19] with typical overpotentials of 150–200 mV whereas the bulk powder exhibits poor catalytic activity. Lower overpotentials of ~100 mV have been reported for amorphous MoS_2 (ref. 17) and by placing nanocrystals on gold[4] or reduced graphene oxide[20] substrates. Further insight into the catalytic activity of the WS_2 electrodes was obtained by extracting the slopes from the Tafel plots shown in Fig. 2b. The lowest Tafel slopes of ~60 mV per decade (or ~55 mV per decade with *iR* correction) were obtained for the 1T WS_2 phase. These values are comparable to those measured for MoS_2 nanoparticles[4,18], suggesting that the surface chemistry mechanisms responsible for HER may be similar even though the geometry and composition are different. Tafel slopes of 40 mV per decade have been reported for MoS_2 nanocrystals on reduced graphene oxide[20]. To quantify the catalytic activity, we measured the actual number of active sites using the copper underpotential deposition method[40] (Supplementary Figs S9 and S10). On the basis of this method, we have determined the number of active sites to be $\sim 4.5 \times 10^{14}$ sites cm^{-2} or higher for the strained 1T phase. The turnover frequency (TOF) of H_2 molecules evolved per second (represented as s^{-1}) was calculated to be 175 s^{-1} at −288 mV for the as-exfoliated monolayered samples, as shown in Fig. 2c. For comparison, the best TOF values reported for molecular catalysts reach about 1,000 s^{-1} at an overpotential of 290 mV and 300 s^{-1} at 725 mV for Ni-bisdiphosphine[41] and molybdenum disulphide[15] complexes. To overcome stability issues associated with such complexes, nickel bisdiphosphine complexes have been attached onto multiwalled carbon nanotubes and assayed at 0.5 M H_2SO_4 (ref. 12). More recently, ref. 42 demonstrated successful grafting of Co-based complexes to multiwalled nanotubes and reported overpotential values of around 350 mV and Tafel slopes of about 160 mV per decade in aqueous electrolyte at neutral pH. In addition to these systems, NiMo and NiMoN catalysts have also been investigated for HER, showing overpotential values ranging from 150 mV to 175 mV (refs 43,44). Pt (111) has an exchange current density (by definition at 0 V) of 4.5×10^{-4} A cm^{-2}, giving a TOF of ~0.9 s^{-1} whereas MoS_2 edges have exchange current densities of $\sim 8 \times 10^{-6}$ A cm^{-2} and a TOF of around 0.02 s^{-1} at pH 0.24 (ref. 4). In comparison, at 0.5 M of H_2SO_4, the exchange current density of exfoliated 1T WS_2 is $\sim 2 \times 10^{-5}$ A cm^{-2} and it has a TOF of ~0.043 s^{-1}. The exact quantification of the active sites and thus the TOF values is challenging in the field of electrocatalysis. The Cu underpotential deposition method used here to determine

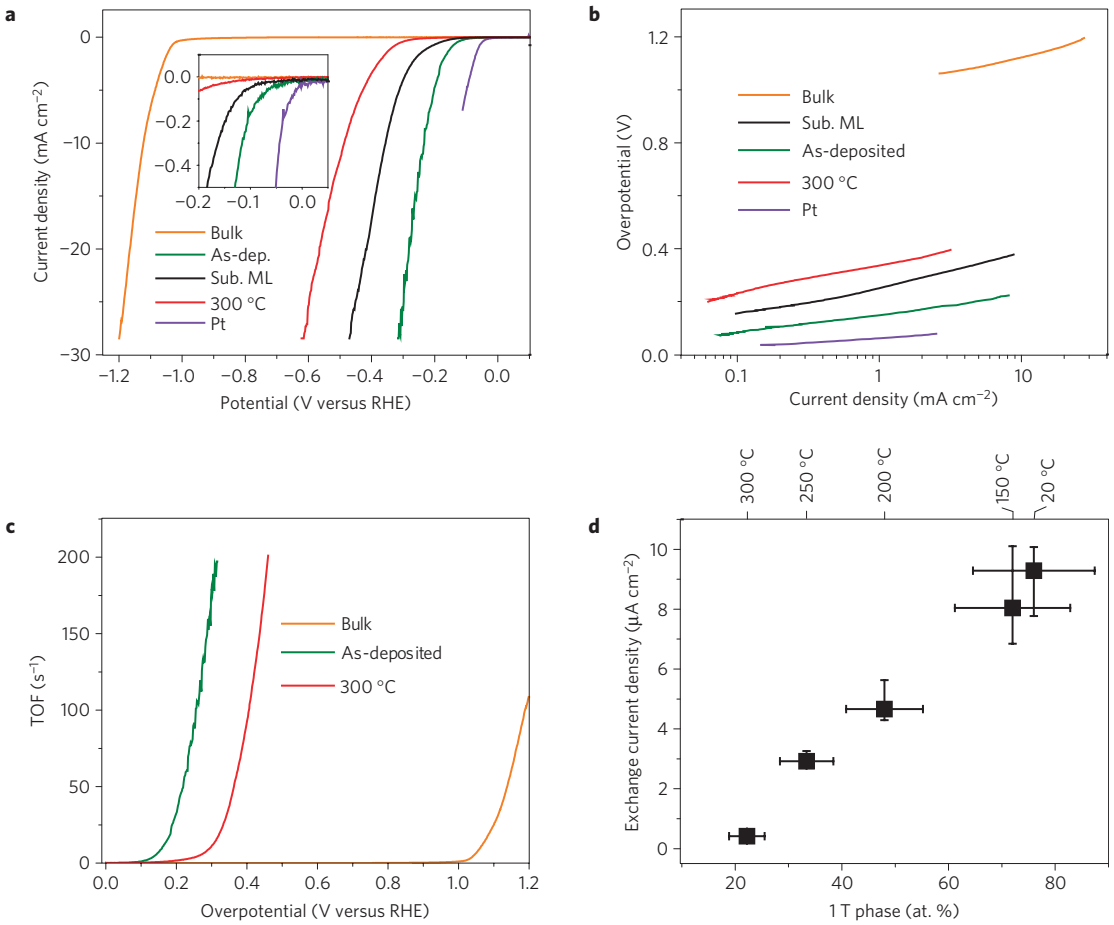

Figure 2 | HER electrocatalytic properties of exfoliated WS_2 nanosheets. Thin films of thicknesses of greater than five monolayers of as-exfoliated 1T and 2H phases of WS_2 nanosheets were deposited onto a glassy carbon electrode. **a**, Polarization curves of bulk and as-exfoliated WS_2 (as-deposited film of 1T phase, sub-monolayer as-exfoliated film, and 2H phase after annealing at 300 °C) along with those corresponding to Pt nanoparticles and bulk WS_2 powder for comparison. **b**, Tafel plots obtained from the polarization curves show significant improvement in the Tafel slope due to exfoliation (60 mV per decade), whereas 2H and bulk samples exhibit much higher values of 110 mV per decade or higher. **c**, TOF as a function of the overpotential for the different materials. The TOF reaches 175 s^{-1} at a potential of −288 mV for as-synthesized WS_2. **d**, Catalytic activity as a function of the 1T phase concentration obtained by annealing in an inert atmosphere. The error bars arise from values extracted from several measurements on multiple samples.

the quantity of active sites is well established for noble metals but further studies are required to confirm that hydrogen and copper adsorb on the same sites on chemically exfoliated WS_2 nanosheets. The measured number of active sites reported here can vary significantly depending on how copper adsorbs onto active and non-active sites, which can lead to significantly different TOF values from those reported here.

The as-exfoliated WS_2 nanosheets contain a high concentration of strained 1T phase metallic regions. To investigate the influence of strain and 1T phase on the catalytic activity, the monolayered WS_2 thin film was incrementally annealed and the catalytic activity after each thermal treatment was measured. This allowed evaluation of catalytic properties of the as-exfoliated WS_2 nanosheets without changing their dimensions or geometrical features. The HER characteristics are strongly linked to both the 1T phase concentration and strain as indicated by a gradual decrease in the exchange current density with increasing 2H fraction and decreasing strain, as shown in Fig. 2d. We have also monitored the HER properties as a function of the proton concentration by varying the pH. The results provided in the Supplementary Information show that above a pH of 0.6 the Tafel slope increases, consistent with a decrease in the concentration of H^+.

An important parameter for viability of a HER catalyst is the electrochemical stability. To investigate stability under electrocatalytic operation, we have measured the HER characteristics of WS_2 catalyst nanosheets by running over 10,000 cycles and monitoring the current density during continuous operation at −0.3 V for more than 100 h. The current density versus time data provided in the Fig. 3a show that the values remain stable after a slight initial decrease (observed for all electrodes including Pt). The variation of the overpotential and concentration of the 1T phase as a function of time are shown in the insets of Fig. 3a. It can be seen that the overpotential does not vary significantly with time after 120 h as indicated by the fact that the 1T phase concentration remains stable during the electrochemical long-term stressing, as indicated by Raman spectroscopy and XPS (Supplementary Fig. S12). Overall, these electrochemical results demonstrate that as-exfoliated WS_2 sheets could be effective electrocatalysts for HER. We have also investigated the impedance of the electrodes and found that it does not change markedly with the addition of 1T or 2H nanosheets to glassy carbon (Supplementary Fig. S14). The measurements show that the resistance of the system is slightly lower for the 1T nanosheets on the glassy carbon electrode, suggesting that in addition to better catalytic activity, charge transfer is also facilitated.

To further investigate the stability of the 1T phase, we have carried out first principles calculations to probe the activation energy for transformation from the 1T to the 2H phase. Specifically,

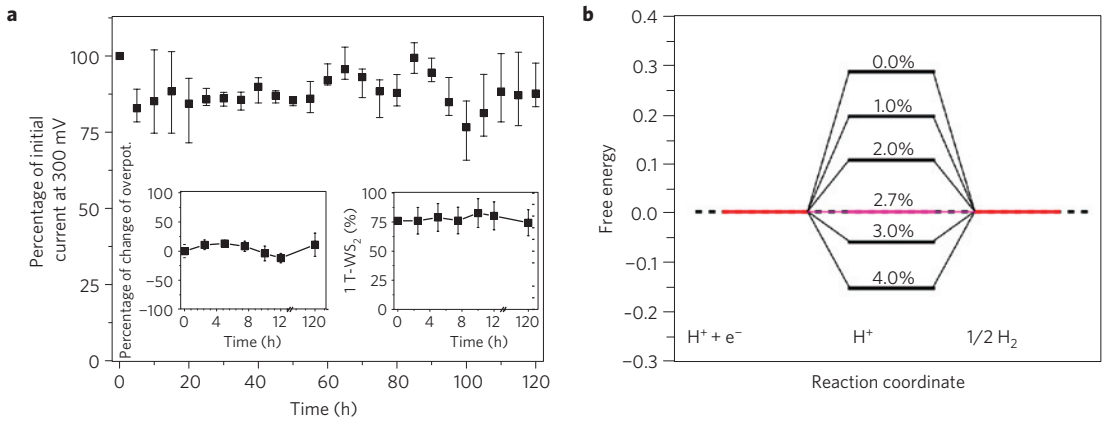

Figure 3 | 1T phase stability and free-energy diagram for hydrogen evolution at equilibrium (U = 0) with tensile strain in atomically thin 1T WS_2. a, The variation in current density versus time (up to 120 h corresponding to >10,000 cycles) of 1T WS_2 electrode operation showing that the current density remains constant over the tested period. The insets show the percentage of change in overpotential (left inset) and variation in 1T phase concentration with time of electrode operation. **b**, The free energy of $H^+ + e^-$ is by definition equal to that of $1/2H_2$ at standard conditions (1 bar of H_2 and pH = 0 at 300 K). The free energies for the intermediate adsorbed state H* are calculated by using DFT and corrected for zero point energies and entropy. The hydrogen coverage of 1/16 S atoms is used for the calculations. The strain 2.7% for zero free energy is obtained by assuming a linear relation between free energy and strain. The error bars in **a** arise from values extracted from several measurements on multiple samples.

we carried out the nudged elastic band calculations to determine the energy barrier of phase transformation between 1T and 2H WS_2. We show that although the 2H WS_2 is more stable with the total energy 0.537 eV lower than that of the 1T WS_2, there is an energy barrier of ~0.95 eV for phase relaxation, as indicated in the Supplementary Information. The calculated energy barrier is consistent with experimental measurements of activation energy (~0.87 eV) for 1T to 2H transformation[34]. The results are also consistent with our observations that the 1T phase remains constant in laboratory-stored samples for over 200 days (Supplementary Fig. S13).

Finally, we performed first-principles calculations to obtain fundamental insight into mechanisms responsible for the very low overpotential and high TOF values for hydrogen evolution in 1T WS_2. The first step in HER is the adsorption of hydrogen onto the catalyst, which can be written as $H^+ + e^- + * \rightarrow H^*$, where $*$ denotes a binding site. The subsequent step is the release of molecular hydrogen by either $2H^* \rightarrow H_2 + 2^*$ or $H^+ + e^- + H^* \rightarrow H_2 + *$ reactions. This process has been theoretically modelled by density functional theory (DFT) calculations and corroborated with experimental results[1,3,4,6]. It is known that a material is a good catalyst when the free energy of adsorbed atomic hydrogen is close to thermoneutral, that is, $\Delta G_H \approx 0$. This is attributed to the fact that if the hydrogen does not efficiently bind to the catalyst or if it forms a strong bond then the proton/electron-transfer step and hydrogen release, respectively, will be inefficient, decreasing catalytic activity. We have calculated the free energy of atomic hydrogen adsorption of distorted 1T WS_2 monolayers as a function of strain. Our calculations show that strain can significantly influence the free energy of atomic hydrogen adsorption on the surface of distorted 1T WS_2 as shown in Fig. 3b. Without strain, the free energy of H adsorption is 0.28 eV. However, the application of tensile strain leads to the enhancement of density of states near the Fermi level that facilitates hydrogen binding (Supplementary Information). As shown in Fig. 3b, the free energy is close to thermoneutral when the strain is varied between 2.0 and 3.0% strain. The free energy equal to zero can be extrapolated for a strain value of 2.7%. These results clearly indicate that the 1T WS_2 phase is catalytically active. For comparison, we have also calculated the effect of strain on catalytic activity of 2H WS_2 and found no improvement in catalytic activity. For example, even with strain as high as 4%, the free energy remained close to ~2 eV, suggesting a very large thermodynamic barrier to HER activity. Furthermore, compressive stress did not have a significant influence on the density of states. It should be noted that although our DFT study provides guidance for interpretation of the results, it does not take into account all of the experimental details. For example, STEM analyses reveal that the 1T WS_2 phase is not uniformly strained. The zigzag pattern shown in Fig. 1b contains both tensile and compressive regions. However, DFT calculations have been performed on ideal 1T nanosheets that are either completely in tension or completely in compression. The results of the calculations show that only those nanosheets in tension are catalytically active whereas those in compression are not. In addition, electrical properties of the nanosheets are also influenced by the variation in the 1T phase and the strain, which plays an important role in the catalytic performance of the nanosheets. That is, DFT calculations do not take into account the charge transfer kinetics. Thus, although DFT results agree well with our experimental results, they should be taken only as a guide.

The present study illustrates the fundamental role of the atomic and electronic structures on the catalytic performance as reported previously for other types of material and reaction. The active forms of cobalt and manganese oxides for water oxidation have a disordered layered structure consisting of molecular clusters with a metal valency greater than 3, whereas more stable and well-ordered structures are found to be less active[45,46]. Our DFT calculations have shown the importance of strain on the electronic structure and as a consequence on the energy of hydrogen adsorption of WS_2. Similarly, in the field of oxygen reduction reaction, the enhanced activity of platinum-transition metal alloys has been attributed to the change of the electronic structure of Pt. The downshift of the *d* band relative to the Fermi level observed in Pt alloys is responsible for making a slightly weaker metal–oxide bond and facilitates the reaction[47]. Finally, the mechanical stability of the electrodes on flexible substrates has been tested in our laboratory for potential use in plastic electronics. We have found that the nanosheets are robust and retain their electrical properties even after hundreds of flexing cycles.

The above experimental and theoretical results suggest that the presence of strain, as confirmed by our HAADF–STEM analysis, and metallic 1T sites are important factors in enhancing catalytic activity of WS_2 nanosheets. The strain induced by zigzag-like local lattice distortions seems to facilitate HER. This combined with the scalability of the solution-based synthesis suggests

that earth-abundant as-exfoliated 1T WS_2 nanosheets could be potentially interesting catalysts for HER.

Methods

Solutions of tungsten disulphide nanosheets were prepared by immersing intercalated WS_2 powder in water. Bulk WS_2 powder was intercalated with lithium by reacting bulk WS_2 powder (0.3 g, Alfa Aesar) with *n*-butyl lithium in hexane (1.6 M, 4 ml, Sigma-Aldrich). The process is comparable to that reported for MoS_2 in ref. 32. More details are provided in the Supplementary Information.

HAADF-STEM imaging was performed using a JOEL JEM-2100F TEM/STEM with double spherical aberration (Cs) correctors (CEOS). The acceleration voltage was 120 kV and the collecting angle was between 100 and 267 mrad. Peak pair analysis to obtain the stress tensor map was conducted with DigitalMicrograph software.

Electrochemical measurements were carried out with a 3-electrode cell using a Versa Stat 3 potentiostat from Princeton Applied Research. Linear sweep voltamperometry with a 5 mV s^{-1} scan rate was performed in 0.5 M H_2SO_4 electrolyte de-aerated with hydrogen, nitrogen or Ar with a saturated calomel electrode (CH Instruments) as the reference electrode, a platinum wire (Alfa Aesar) as the counter electrode and a glassy carbon electrode (CH Instruments) as the working electrode. The same measurements were performed using a carbon counter electrode to rule out any Pt contamination when using a platinum counter electrode. The polarization curves from either counter electrodes are identical as shown in Supplementary Fig. S15. The reference electrode was calibrated for the reversible hydrogen potential using platinum wire as working and counter electrodes in the electrolyte solution saturated with H_2. In 0.5 M H_2SO_4, E (RHE) = E (SCE) + 0.213 V. The site density measurements were carried out using the underpotential deposition method of ref. 40. Alternating current impedance measurements were performed in the same configuration at +0.1 V from 10^6 to 0.85 Hz with an a.c. voltage of 5 mV. Samples were directly deposited or transferred after annealing on the working electrode. WS_2 was loaded onto the glassy carbon surface at 0.1–0.2 μg cm^{-2} (or approximately one continuous layer of WS_2 over the 1 cm^2 electrode surface area) to 6.5 μg cm^{-2} and dried. Then, 7 μl of 5% Nafion solution in ethanol was drop-cast on top to protect the WS_2 film. To prepare 2H WS_2 samples, exfoliated WS_2 was annealed first before the transfer on the working electrode. See Supplementary Information for more details.

The DFT calculations were carried out by using the Vienna *ab initio* simulation package[48], with the exchange-correlation functional described by the Perdew–Burke–Ernzerhof generalized gradient approximation[49] and interaction between core electrons and valence electrons by the frozen-core projector-augmented wave method[50]. An energy cutoff of 600 eV was used for plane wave basis expansion. More details are given in the Supplementary Information.

Received 3 December 2012; accepted 29 May 2013; published online 7 July 2013

References

1. Greeley, J. *et al.* Computational high-throughput screening of electrocatalytic materials for hydrogen evolution. *Nature Mater.* **5,** 909–913 (2006).
2. Laursen, L. B., Kegnæs, S., Dahla, S. & Chorkendorff, I. Molybdenum sulfides efficient and viable materials for electro- and photoelectrocatalytic hydrogen evolution. *Energy Environ. Sci.* **5,** 5577–5591 (2012).
3. Hinnemann, B. *et al.* Biomimetic hydrogen evolution: MoS_2 nanoparticles as catalyst for hydrogen evolution. *J. Am. Chem. Soc.* **127,** 5308–5309 (2005).
4. Jaramillo, T. F. *et al.* Identification of active edge sites for electrochemical H_2 evolution from MoS_2 nanocatalysts. *Science* **317,** 100–102 (2007).
5. Jaramillo, T. F. *et al.* Hydrogen evolution on supported incomplete cubane-type $[Mo_3S_4]^{4+}$ electrocatalysts. *J. Phys. Chem. C* **112,** 17492–17498 (2008).
6. Bonde, J. *et al.* Hydrogen evolution on nano-particulate transition metal sulfides. *Faraday Discuss.* **140,** 219–231 (2008).
7. Nørskov, J. K., Bligaard, T., Rossmeisl, J. & Christensen, C. H. Towards the computational design of solid catalysts. *Nature Chem.* **1,** 37–46 (2009).
8. Subbaraman, R. *et al.* Enhancing hydrogen evolution activity in water splitting by tailoring Li^+-Ni $(OH)_2$–Pt interfaces. *Science* **334,** 1256–1260 (2011).
9. Hou, Y. *et al.* Bioinspired molecular co-catalysts bonded to a silicon photocathode for solar hydrogen evolution. *Nature Mater.* **10,** 434–438 (2011).
10. Seger, B. *et al.* Hydrogen production using a molybdenum sulfide catalyst on a titanium-protected n+p-silicon photocathode. *Angew. Chem. Int. Ed.* **51,** 9128–9131 (2012).
11. Bollinger, M. V. *et al.* One-dimensional metallic edge states in MoS_2. *Phys. Rev. Lett.* **87,** 196803 (2001).
12. Le Goff, A. *et al.* From hydrogenases to noble metal-free catalytic nanomaterials for H_2 production and uptake. *Science* **326,** 1384–1387 (2009).
13. Karunadasa, H. I., Chang, C. J. & Long, J. R. A molecular molybdenum-oxo catalyst for generating hydrogen from water. *Nature* **464,** 1329–1333 (2010).
14. Helm, M. L., Stewart, M. P., Bullock, R. M., Rakowski DuBois, M. & DuBois, D. L. A synthetic nickel electrocatalyst with a turnover frequency above 100,000 s^{-1} for H_2 production. *Science* **333,** 863–866 (2011).
15. Karunadasa, H. I. *et al.* A molecular MoS_2 edge site mimic for catalytic hydrogen generation. *Science* **335,** 698–702 (2012).
16. Merki, D., Fierro, S., Vrubel, H. & Hu, X. Amorphous molybdenum sulfide films as catalysts for electrochemical hydrogen production in water. *Chem. Sci.* **2,** 1262–1267 (2011).
17. Vrubel, H., Merki, D. & Hu, X. Hydrogen evolution catalyzed by MoS_3 and MoS_2 particles. *Energy Environ. Sci.* **5,** 6136–6144 (2012).
18. Chen, Z. *et al.* Core shell MoO_3–MoS_2 nanowires for hydrogen evolution: A functional design for electrocatalytic materials. *Nano Lett.* **11,** 4168–4175 (2011).
19. Kibsgaard, J., Chen, Z., Reinecke, B. N. & Jaramillo, T. F. Engineering the surface structure of MoS_2 to preferentially expose active edge sites for electrocatalysis. *Nature Mater.* **11,** 963–969 (2012).
20. Li, Y. *et al.* MoS_2 nanoparticles grown on graphene: An advanced catalyst for the hydrogen evolution reaction. *J. Am. Chem. Soc.* **133,** 7296–7299 (2011).
21. Joensen, P., Frindt, R. F. & Morrison, S. R. Single-layer MoS_2. *Mater. Res. Bull.* **21,** 457–461 (1986).
22. Novoselov, K. S. *et al.* Two-dimensional atomic crystals. *Proc. Natl Acad. Sci. USA* **102,** 10451–10453 (2005).
23. Splendiani, A. *et al.* Emerging photoluminescence in monolayer MoS_2. *Nano Lett.* **10,** 1271–1275 (2010).
24. Coleman, J. N. *et al.* Two-dimensional nanosheets produced by liquid exfoliation of layered materials. *Science* **331,** 568–571 (2011).
25. Zhan, Y. *et al.* Large-area vapor-phase growth and characterization of MoS_2 atomic layers on a SiO_2 substrate. *Small* **8,** 966–971 (2012).
26. Liu, K. K. *et al.* Growth of large-area and highly crystalline MoS_2 thin layers on insulating substrates. *Nano Lett.* **12,** 1538–1544 (2012).
27. Lee, Y-H. *et al.* Synthesis of large-area MoS_2 atomic layers with chemical vapor deposition. *Adv. Mater.* **24,** 2320–2325 (2012).
28. Chang, Y-H. *et al.* Highly efficient electrocatalytic hydrogen production by MoS_x grown on graphene-protected 3D Ni foams. *Adv. Mater.* **5,** 756–760 (2012).
29. Radisavljevic, B., Radenovic, A., Brivio, J., Giacometti, V. & Kis, A. Single-layer MoS_2 transistors. *Nature Nanotech.* **6,** 147–150 (2011).
30. Li, T. & Galli, G. Electronic properties of MoS_2 nanoparticles. *J. Phys. Chem. C* **111,** 16192–16196 (2007).
31. Mak, K. F., Lee, C., Hone, J., Shan, J. & Heinz, T. F. Atomically thin MoS_2: A new direct-gap semiconductor. *Phys. Rev. Lett.* **105,** 136805 (2010).
32. Eda, G. *et al.* Photoluminescence from chemically exfoliated MoS_2. *Nano Lett.* **11,** 5111–5116 (2011).
33. Py, M. A. & Haering, R. R. Structural destabilization induced by lithium intercalation in MoS_2 and related compounds. *Can. J. Phys.* **61,** 76–84 (1983).
34. Tsai, H-L., Heising, J., Schindler, J. L., Kannewurf, C. R. & Kanatzidis, M. G. Exfoliated-restacked phase of WS_2. *Chem. Mater.* **9,** 879–882 (1997).
35. Paracchino, A., Laporte, V., Sivula, K., Grätzel, M. & Thimse, E. Highly active oxide photocathode for photoelectrochemical water reduction. *Nature Mater.* **10,** 456–461 (2011).
36. Miremadi, B. K. & Morrison, S. R. The intercalation and exfoliation of tungsten disulfide. *J. Appl. Phys.* **63,** 4970–4974 (1988).
37. Heising, J. & Kanatzidis, M. G. Structure of restacked MoS_2 and WS_2 elucidated by electron crystallography. *J. Am. Chem. Soc.* **121,** 638–643 (1999).
38. Galindo, P. L. *et al.* The peak pairs algorithm for strain mapping from HRTEM images. *Ultramicroscopy.* **107,** 1186–1193 (2007).
39. Yang, D. & Frindt, R. F. Li-intercalation and exfoliation of WS_2. *J. Phys Chem Solids.* **57,** 1113–1116 (1996).
40. Green, C. L. & Kucernak, A. Determination of the platinum and ruthenium surface areas in platinum–ruthenium alloy electrocatalysts by underpotential deposition of copper. I. Unsupported catalysts. *J. Phys. Chem. B* **106,** 1036–1047 (2002).
41. Kilgore, U. J. *et al.* $[Ni(PPh_2NC_6H_4X_2)_2]^{2+}$ complexes as electrocatalysts for H_2 production: Effect of substituents, acids, and water on catalytic rates. *J. Am. Chem. Soc.* **133,** 5861–5872 (2011).
42. Andreiadis, E. S. *et al.* Molecular engineering of a cobalt-based electrocatalytic nanomaterial for H_2 evolution under fully aqueous conditions. *Nature Chem.* **5,** 48–53 (2013).
43. McKone, J. R. *et al.* Evaluation of Pt, Ni, and Ni–Mo electrocatalysts for hydrogen evolution on crystalline Si electrodes. *Energy Environ. Sci.* **4,** 3573–3583 (2011).
44. Chen, W-F. *et al.* Hydrogen-evolution catalysts based on non-noble metal nickel–molybdenum nitride nanosheets. *Angew. Chem. Int. Ed.* **51,** 6131–6135 (2012).
45. Kanan, M. W. *et al.* Structure and valency of a cobalt–phosphate water oxidation catalyst determined by *in situ* X-ray spectroscopy. *J. Am. Chem. Soc.* **132,** 13692–13701 (2010).
46. Zaharieva, I. *et al.* Synthetic manganese–calcium oxides mimic the water-oxidizing complex of photosynthesis functionally and structurally. *Energy Env. Sci.* **4,** 2400–2408 (2011).

47. Stamenkovic, V. *et al.* Changing the activity of electrocatalysts for oxygen reduction by tuning the surface electronic structure. *Angew. Chem. Int. Ed.* **45,** 2897–2901 (2006).
48. Kresse, G. & Furthmuller, J. Efficient iterative schemes for *ab initio* total-energy calculations using a plane-wave basis set. *Phys. Rev. B* **54,** 11169–11186 (1996).
49. Perdew, J. P., Burke, K. & Ernzerhof, M. Generalized gradient approximation made simple. *Phys. Rev. Lett.* **77,** 3865–3868 (1996).
50. Blöchl, P. E. Projector augmented-wave method. *Phys. Rev. B* **50,** 17953–17979 (1994).

Acknowledgements

M. Chhowalla acknowledges financial support from NSF DGE 0903661. H.Y. acknowledges the Japan Society for the Promotion of Science (JSPS) for financial support through Postdoctoral Fellowship for Research Abroad. G.E. acknowledges financial support from NRF Singapore. J.L. and V.B.S. acknowledge support from Army Research Office through Contract W911NF-11-1-0171. T.A. acknowledges financial assistance from NSF (CAREER CHE-1004218, DMR-0968937, NanoEHS-1134289, NSF-ACIF, and Special Creativity Grant). R.S. and D.C.B.A. acknowledge the Coordenação de Aperfeiçoamento de Pessoal de Nível Superior, Brazil for fellowships. R.S. also acknowledges the Fulbright Agency, USA for financial support. T.F. acknowledges partial support from JST-PRESTO 'New Materials Science and Element Strategy' and JSPS, Grant-in-Aid for challenging Exploratory Research (24656028). We thank M. Salehi for the AFM images.

Author contributions

M. Chhowalla conceived the idea, designed the experiments, analysed the data and wrote the manuscript. D.V. conceived the idea and designed the experiments with M. Chhowalla, synthesized the WS_2 nanosheets, characterized them with AFM, Raman and XPS, performed the HER measurements and analysed the data. H.Y. assisted in the synthesis and characterization of materials. J.L. and V.S. performed the theoretical work. T.F. and M. Chen performed the TEM work. R.S., D.C.B.A. and T.A. assisted D.V. with the HER measurements. G.E. analysed the TEM and strain data as well as editing the manuscript. All of the authors have read the manuscript and agree with its content.

Additional information

Supplementary information is available in the online version of the paper. Reprints and permissions information is available online at www.nature.com/reprints. Correspondence and requests for materials should be addressed to M.C.

Competing financial interests

The authors declare no competing financial interests.